

## Article

# Distinct Evidence of Hydrogen-Enhanced Defect Formation on Pre-Strained Nickel Alloy 625 during In Situ Electrochemical Nanoindentation Test

Chandrahasan K. Soundararajan <sup>1,\*</sup>, Xu Lu <sup>1</sup>, Dong Wang <sup>1</sup>  and Alexei Vinogradov <sup>2</sup> 

<sup>1</sup> Department of Mechanical and Industrial Engineering, Norwegian University of Science and Technology, No-7491 Trondheim, Norway

<sup>2</sup> Magnesium Research Center (MRC), Kumamoto University, 2-39-1 Kurokami, Chuo-ku, Kumamoto 860-8555, Japan

\* Correspondence: chandrahasan.k.soundararajan@ntnu.no

**Abstract:** In the present work, in situ electrochemical nanoindentation was utilized to investigate the hydrogen effect on the nanomechanical properties of tensile pre-strained nickel alloy (0%, 5% and 20%). The study reveals that hydrogen-induced hardening occurs during cathodic polarization due to hydrogen incorporation and softening behavior during anodic polarization; this is due to the irreversible microstructure modification induced in the presence of hydrogen solutes. Their respective contributions were quantified by fitting the elastoplastic part of the load-displacement data. In addition, the differences in their plastic behaviors were investigated in detail by examining the dislocation structure underneath the indents. This study aims to shed light on hydrogen's interaction with pre-existing defects.

**Keywords:** in situ nanoindentation; hydrogen; pre-strain nickel alloy; hardening and softening; dislocations; defect formation



**Citation:** Soundararajan, C.K.; Lu, X.; Wang, D.; Vinogradov, A. Distinct Evidence of Hydrogen-Enhanced Defect Formation on Pre-Strained Nickel Alloy 625 during In Situ Electrochemical Nanoindentation Test. *Metals* **2024**, *14*, 161. <https://doi.org/10.3390/met14020161>

Academic Editor: Tomáš Prošek

Received: 18 November 2023

Revised: 23 January 2024

Accepted: 26 January 2024

Published: 28 January 2024



**Copyright:** © 2024 by the authors. Licensee MDPI, Basel, Switzerland. This article is an open access article distributed under the terms and conditions of the Creative Commons Attribution (CC BY) license (<https://creativecommons.org/licenses/by/4.0/>).

## 1. Introduction

Strain hardening is a common technique used to enhance the load-bearing capacity of structural materials. In a hydrogen environment, the deformed structures are particularly vulnerable to hydrogen embrittlement (HE). Different HE damage mechanism models have been proposed based on observations from various annealed materials, essentially describing the interaction between hydrogen and microstructural defects [1–4]. However, the HE behavior of plastically pre-strained material is even more complex to describe due to the persistent evolution of microstructural heterogeneities (e.g., dislocations, twins, vacancies, etc.) with plastic strain and the varied hydrogen effect on each stage.

For instance, in small tensile plastic strains, hydrogen-induced hardening is reported in nickel due to the formation of Cottrell atmospheres, resulting in a solute drag effect, whereas in large plastic strains, the softening behavior is observed due to the shielding effect [5–7]. During plastic deformation, strain-induced vacancies are generated through the dislocation interactions, such as cutting the screw dislocations and annihilations of edge segments of opposite signs located on the same slip plane. Under plastic straining in the presence of hydrogen, the vacancy concentration is shown to exceed the equilibrium concentration, which can subsequently impact the dislocation mobility and influence the diffusion and trapping behavior [8,9].

For a comprehensive understanding of damage mechanisms in a pre-strained material, detailed knowledge of hydrogen diffusion and trapping, as well as their interaction with pre-existing defects such as dislocations, vacancies, etc., is required. An earlier work from the author's group has investigated hydrogen diffusion and trapping in pre-strained nickel alloy 625 [10]. The study revealed that the hydrogen diffusivity in pre-strained samples is

mainly controlled by the competition between trap density (dislocations, grain boundary carbides) and the availability of the fast diffusion path, primarily along the regions adjacent to grain boundaries (plastic strain-induced vacancies, hydrogen charging-induced vacancy clusters). The preferential formation of hydrogen-enhanced strain-induced vacancy clusters close to grain boundary regions has also been reported in Ni-201 alloy [9]. Additionally, Oudriss et al. reported that, in the case of pre-strained pure nickel, the initial concentration of vacancies plays a key role in the formation of new vacancies by hydrogen during permeation experiments [11]. A common consensus among these studies is that hydrogen facilitates the dynamic evolution of lattice defects; however, the prerequisites for such a process remain unclear. Thus, the aim of this work is to investigate the damage mechanism in the pre-strained nickel alloy 625 using the in situ electrochemical nanoindentation technique (ECNI), which offers a unique advantage when examining the fundamental mechanisms associated with the influence of hydrogen on the mechanical behavior of materials in a controllable hydrogen atmosphere.

While considerable research in nanoindentation has focused on assessing the hydrogen-induced changes in nanomechanical properties of well-annealed ductile materials [12–14], information regarding the hydrogen effect on pre-strained materials is still scarce [6,15,16]. In this work, we have designed an experiment that captures the hydrogen effect on the material response after two hours of cathodic charging, while the nanomechanical properties obtained after one hour of anodic discharging provide insights into the aftereffects of hydrogen-affected microstructure changes. By integrating these findings, our results shed light on the interplay between hydrogen uptake, prior deformation, microstructure changes, and plastic deformation, providing a comprehensive understanding of the underlying mechanisms that govern hydrogen embrittlement in pre-strained nickel alloy.

## 2. Methodology

### 2.1. Sample Preparation and Microstructure Characterization

To investigate the effect of prior deformation on the hydrogen-affected behavior of the Inconel 625 nickel alloy, flat tensile specimens with a gauge dimension of  $3 \times 16 \times 32$  mm (thickness  $\times$  width  $\times$  length) were pre-strained under uniaxial tension in air up to two nominal strain levels ( $\epsilon$ ): 5% and 20%, using the MTS Series 809 Test System. Disk specimens of 12 mm in diameter were machined out from the gauge part of both plastically deformed samples using an electrical discharge machine. The fabricated disc samples were mechanically ground and polished down to 200 nm colloidal silica to obtain a deformation-free surface. Microstructural examination using the electron channeling contrast imaging (ECCI) technique was carried out before and after indentation using the Quanta 650 FEG microscope (Thermo Fisher Inc., Waltham, MA, USA) operated at an accelerating voltage of 20 keV and at a working distance of 7 mm. To study the dislocation structure underneath the indents, a transmission electron microscopy (TEM) analysis was performed on the lamella prepared using the focused ion beam milling (FIB) technique with a final thickness of about a few tens of nm.

### 2.2. ECNI and Hydrogen Content Measurement

An ECNI experiment was performed using a Bruker TI 950 Triboindenter (Bruker, Billerica, MA, USA) under the load-controlled mode using a Berkovich indenter. The maximum load was set at 2000  $\mu$ N, and the loading and unloading rate was 8000  $\mu$ N/s. The hold segment (0.6 s) at maximum load is used to determine if there is time dependent plasticity or creep in the material, with an additional 0.25 s holding time at 10% of the peak load during unloading for thermal drift correction. The electrochemical charging cell comprises a platinum sheet as a counter electrode (anode), the test specimen as a cathode, and Hg/Hg<sub>2</sub>SO<sub>4</sub> as a reference electrode with a glycerol and borax mixture used as an electrolyte. The experimental sequence for indentation was as follows: At first, the indents were made in air (H-free condition). Then, the samples were electrochemically charged at a constant cathodic current density of  $-0.1$  mA/cm<sup>2</sup> for two hours to allow sufficient

hydrogen to penetrate into the specimen, and then indents were performed. Subsequently, the potential was changed to anodic (0 mV for 1 h) to study the time effect/hydrogen desorption on the nanomechanical properties. For each condition, at least 50 indents were produced on the randomly chosen region. Since the objective of this work is to investigate the hardening behavior, the effect of grain orientation is not considered here. The total hydrogen content was measured using the Bruker G4 Phoenix DH hydrogen analyzer. Note that the hydrogen contents reported in Table 1 represent a similar charging history to that of the indentation experiment.

**Table 1.** Total hydrogen content in pre-strained samples after charging under different conditions.

Sample ID	Charging Condition and Duration	Total Hydrogen Content (wt. ppm)
0%—H	−0.1 mA/cm <sup>2</sup> / 2 h	0.49
0%—Anodic	−0.1 mA/cm <sup>2</sup> /2 h (+) 0 mV/1 h	0.15
5%—H	−0.1 mA/cm <sup>2</sup> /2 h	0.79
5%—Anodic	−0.1 mA/cm <sup>2</sup> /2 h (+) 0 mV/1 h	0.23
20%—H	−0.1 mA/cm <sup>2</sup> /2 h	1.07
20%—Anodic	−0.1 mA/cm <sup>2</sup> /2 h (+) 0 mV/1 h	0.36

### 3. Results and Discussion

#### 3.1. Microstructure of the Pre-Strained 625 Nickel Alloy

Figure 1a shows the engineering stress–strain curve for the nickel-based alloy 625. The pre-strain levels of 5% and 20% are marked by rectangles. Figure 1b–d shows the back-scattered electron images of the initial microstructure and the pre-deformed microstructure prior to indentation. Plastic deformation induces various defects, such as vacancies and dislocations, acting as traps for hydrogen atoms. With the increasing pre-strain, the trap density increases, thereby promoting more hydrogen uptake (Table 1), which is consistent with earlier studies focusing on hydrogen diffusion in different alloy systems: DP steels [17], carbon steels [18], nickel alloys [10,11].

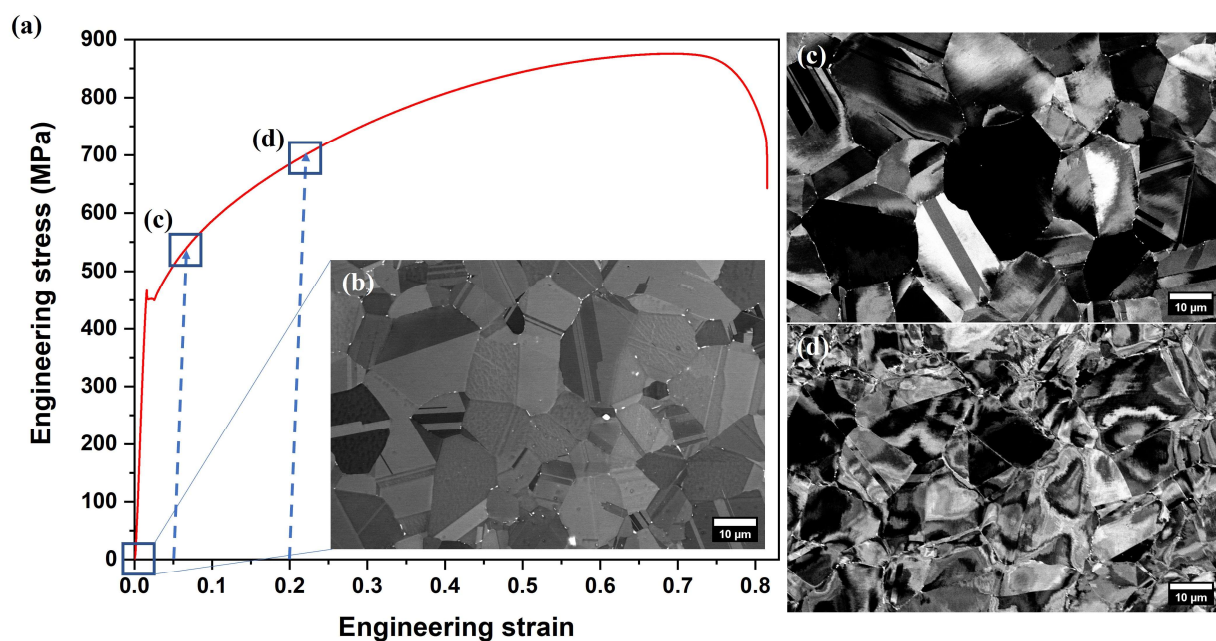


**Figure 1.** (a) Engineering stress–strain plot for nickel alloy 625 (the blue square highlights the pre-strain value used for this study). (b–d) BSE micrographs showing typical fragments of the microstructure: (b) undeformed sample, (c) 5% pre-strain, (d) 20% pre-strain.

### 3.2. Nanomechanical Properties

The majority of the nanoindentation research was focused on probing the pop-in stage to investigate the change in the dislocation nucleation stress during hydrogen charging [19,20]. In the present work, no distinct pop-in stage was observed in pre-strained samples, evidently due to pre-existing defects making the homogeneous dislocation nucleation difficult and masking the pop-in behavior. Therefore, we confine ourselves to the examination of the hardening/softening response of the pre-strained nickel alloy in a hydrogen environment.

For the present study, the hardness of the material was estimated by fitting the unloading curve of the load-displacement (LD) plot using the Oliver–Pharr method [21]. Figure 2a shows the average hardness value for different pre-strained samples subjected to the same charging history, and Figure 2b shows the corresponding cumulative probability plot. For the tests in air (H-free condition), the hardness of the 5% pre-strain sample does not vary much in comparison with that of the original material. During nanoindentation, only a small fraction of the sample is tested (the area of a few hundred nanometers size). Thus, only the defects located directly under the indenter can exert a strong influence on the indentation response. Even though the difference in the average dislocation density ( $\rho_{SSD}$ ) for the 5% pre-strained sample is two orders of magnitude larger than that in the undeformed sample (c.f., Table 2), and the microscopic dislocation distribution is inhomogeneous. Furthermore, the dislocation density can be used as a state variable only when a whole sample is stressed/strained. During nanoindentation testing, this condition is not met due to the strongly localized stress field beneath the sharp indenter and the probabilistic nature of finding the defects in the deformation zone created by the indenter [22–24]. Thus, for 5% pre-strained material, either the probed area is defect-free or, due to very high localized stress generated under the indenter, the defect strength is nullified. Similar findings have been reported for cyclically pre-strained pure nickel with a dislocation density comparable to our measured value [6,15]. On the other hand, the 20% pre-strain sample exhibits an increased hardness value (11% larger) when compared to the undeformed sample. The corresponding microstructure (Figure 1d) shows a nearly uniform dislocation distribution. Thus, the likelihood of the indenter encountering pre-existing defects is increased, resulting in high hardness [22].

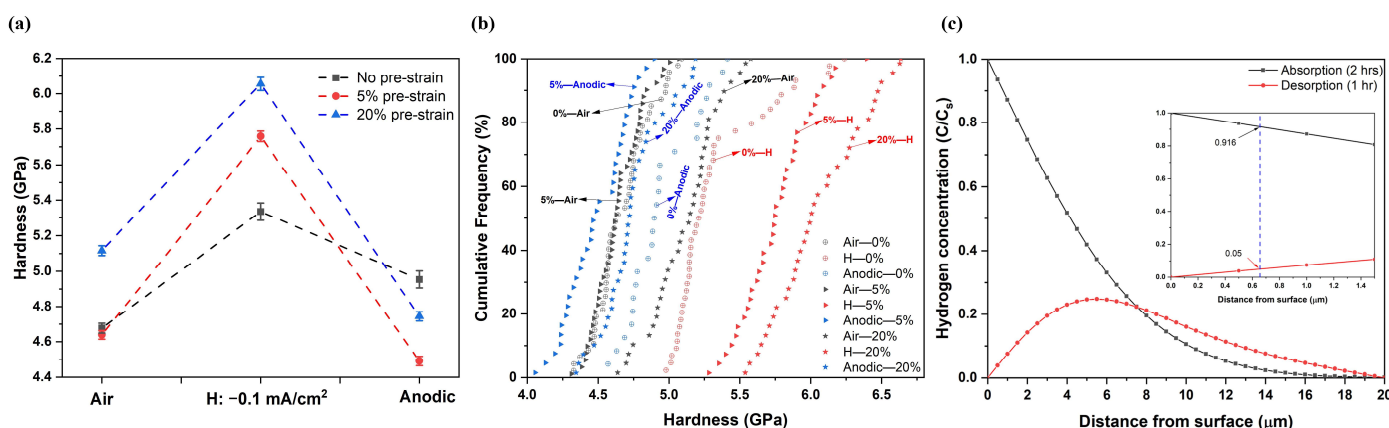


**Figure 2.** (a) Hardness data for three different samples. (b) Corresponding cumulative frequency plot of hardness data for all samples. (c) Hydrogen diffusion–desorption profile for the 5% pre-strained sample after two hours of charging and one hour of desorption. The inset in (c) shows the enlarged view of the hydrogen profile pertaining to the deformation depth. The relations used to plot the diffusion–desorption profile are provided in Appendix A.

While there is an obvious increase in the hardness value for all samples during hydrogen incorporation, the degree of hardening is more prominent for the pre-strained samples. ECC images of indents performed at different charging conditions are shown in Figure 3.

The dislocations here appear as white lines or bright spots on the dark background. The size of the plastic zone ( $R_c$ ) marked by a red circle in Figure 3a indicates the region of the greatest dislocation population around the indent's footprint. A substantial decrease in the  $R_c$  value (see bottom left) is seen during hydrogen charging, and the reduction is more pronounced with the increase in pre-strain. This trend is consistent with the hardness response. It is also noticeable that there is an extensive material pile up close to the indent in the hydrogenated samples, suggesting enhanced strain hardening [13,25,26]. H-induced hardening can be further explained in such a way that the H solute accumulates around the edge components of a dislocation loop or dipole and can exert a pinning effect which resembles a Cottrell atmosphere. An increase in the constraint to dislocation motion is the result of the pinning effect [13,15,27]. H-induced resistance to dislocation motion, and the interpretation of the solid solution hardening mechanism with hydrogen, is considered as an alloying element and was also reported by Ogawa et al. [28]. Similar results were reported during in situ testing of the cyclically pre-strained pure nickel [15] and in the discrete dislocation dynamics computer simulation [29].

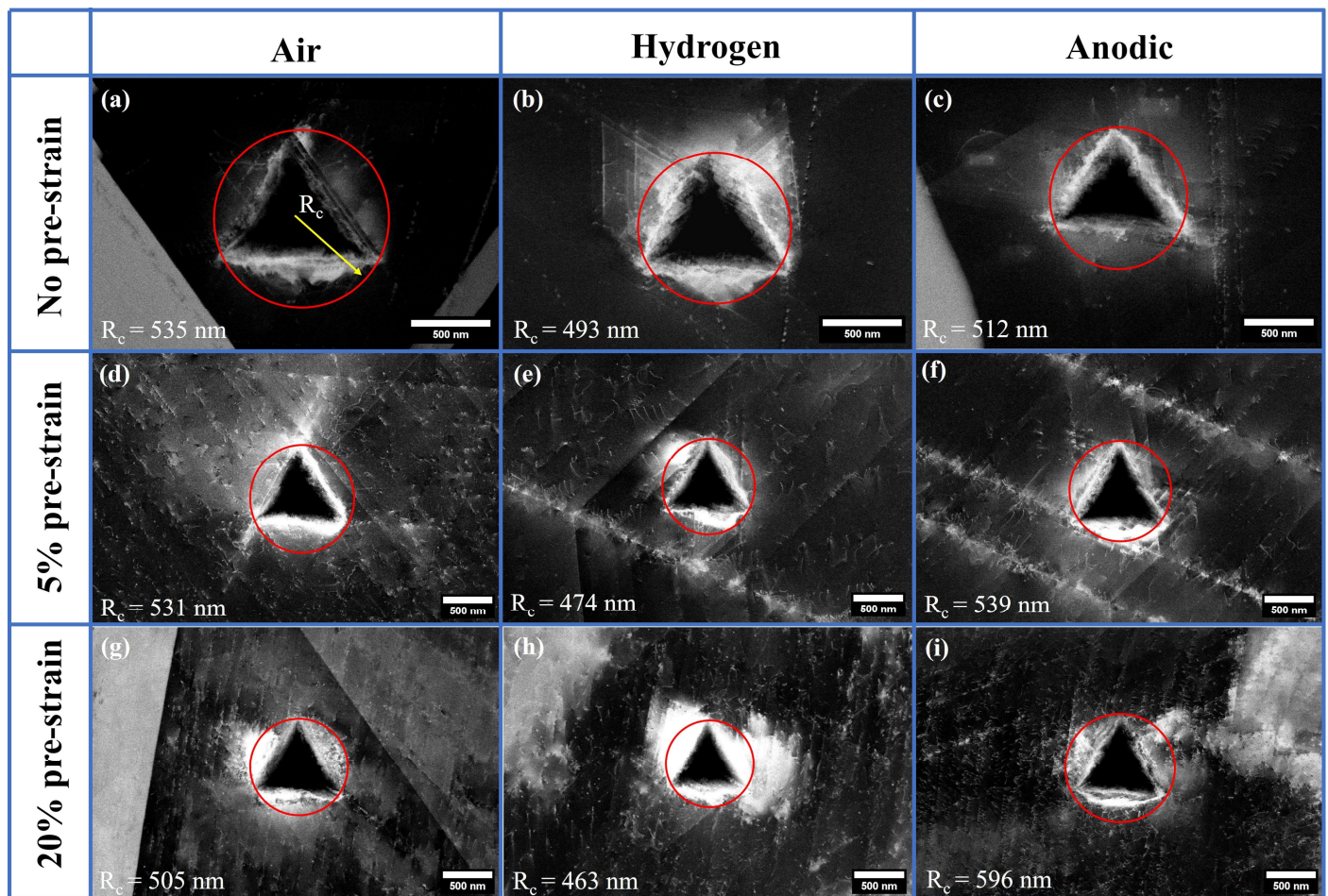


**Figure 3.** ECC images of indents performed at different charging conditions for three different samples. (a–c) indents correspond to undeformed sample. (d–f) indents correspond to 5% pre-strained sample. (g–i) indents correspond to 20% pre-strained sample. (a,d,g) indents performed in air. (b,e,h) indents performed in hydrogen. (c,f,i) indents performed under anodic condition. The plastic zone size ( $R_c$ ), which signifies extensive plastic deformation around the indents, is marked by the red circle, and the corresponding  $R_c$  values measured for each indent are shown on the bottom-left.

When the potential is changed to anodic, the hardness of the undeformed sample has not completely recovered to the same level as that in air (6% increase). From the diffusion–desorption profile (see Table A1), we can see that the remaining hydrogen, after a sequence of two hours of charging and one hour of discharging at a depth of 650 nm, is approximately 5.3%. Thus, the incomplete recovery of the hardness in the initial material is due to the presence of residual hydrogen [13,30]. Interestingly, for the pre-strained materials, the hardness during anodic discharging is much lower than that of the indents performed in air (3% and 7% decrease for 5% and 20% pre-strain, respectively), even though the diffusion–desorption profile (Figure 3c) and the hydrogen content measurement (Table 1) suggest the presence of residual solute after the anodic sequence. Moreover, the  $R_c$  value during the anodic polarization sequence reveals an increasing trend with the increase in pre-strain, thus suggesting the softening behavior.

The elastoplastic part of the load–displacement curve represents the continuous hardening process. To quantify the hydrogen-induced hardening/softening, the modified Tabor relation-based Nix–Gao model is used to fit the elastoplastic part using the relation shown in Equation (1); for a detailed derivation of this relation, readers are encouraged to refer to our earlier work [30].

$$P = CM\alpha GbA_c \sqrt{\rho_{SSD} + \rho_{GND}} + C(\sigma_{ss} + \sigma_H)A_c \quad (1)$$

where  $C$  is the Tabor constant,  $M$  is the texture dependent Taylor orientation factor converting the shear stress to the axial one,  $\alpha$  is an empirical factor of 0.2–0.5 depending on the dislocation arrangement,  $G$  is the shear modulus,  $b$  is the magnitude of the Burger’s vector of the dislocation,  $A_c$  is the projected area that depends on the indentation depth ( $h$ ) and indenter shape, and  $\rho_{SSD}$  is the density of statistically stored dislocations. The  $\rho_{GND}$  refers to the density of geometrically necessary dislocations; it can be calculated according to the Nix–Gao model [31] as  $\rho_{GND} = \frac{3}{2} \frac{1}{f^3} \frac{\tan^2 \theta}{bh}$ , where  $f$  is the fitting parameter. The  $f$  value serves as a measure of the extent of plastic deformation and represents the ratio between the radius of the plastic zone  $R_c$  and contact area  $a_c$ .  $\theta$  is the angle between the sample surface and Berkovich indenter (24.63°). The  $\sigma_{ss}$  value is the anticipated solid solution strengthening stress, which is numerically equal to approximately 330 MPa [12,30], and  $\sigma_H$  is the additional solid solution strengthening contribution provided by hydrogen; for the uncharged sample (air), this term can be neglected. The summary of physical constants is reported in Table 2. By fitting Equation (1) to the load–displacement data, the hydrogen-induced frictional contribution ( $\sigma_H$ ) is obtained for each sample as shown in Figure 4.

The analysis of the elastoplastic part of the load–displacement curves provides valuable information on the hydrogen-induced frictional stress ( $\sigma_H$ ) for dislocation motion, which has been demonstrated in Figure 4d. The positive stress value indicates a hardening effect, while a negative value indicates a softening effect. For pre-strained samples with surface slip lines induced by H-charging, a larger  $\sigma_H$  was obtained through fitting, and it increases with pre-strain. It is also evident that the increase in frictional stress is linearly dependent on the hydrogen concentration. A similar result has been reported in the earlier work on the pristine (undeformed) microstructure [30]. The hydrogen solute accumulation at the pre-existing lattice defect sites acts as an obstacle to mobile dislocations, i.e., it provides a constraint to dislocation loop expansion, resulting in hydrogen-induced hardening [27].

**Table 2.** Physical constants used in this work to model the elastoplastic part.

C	M	$\alpha$	G (GPa) [30]	b (nm) [30]	$\sigma_{ss}$ (MPa) [12,30]	$\rho_{SSD}$ (/m <sup>2</sup> ) [10]		
						No pre-strain	5% pre-strain	20% pre-strain
3	3.06	0.5	80	0.253	330	$4 \times 10^{12}$	$1.5 \times 10^{14}$	$1.6 \times 10^{15}$

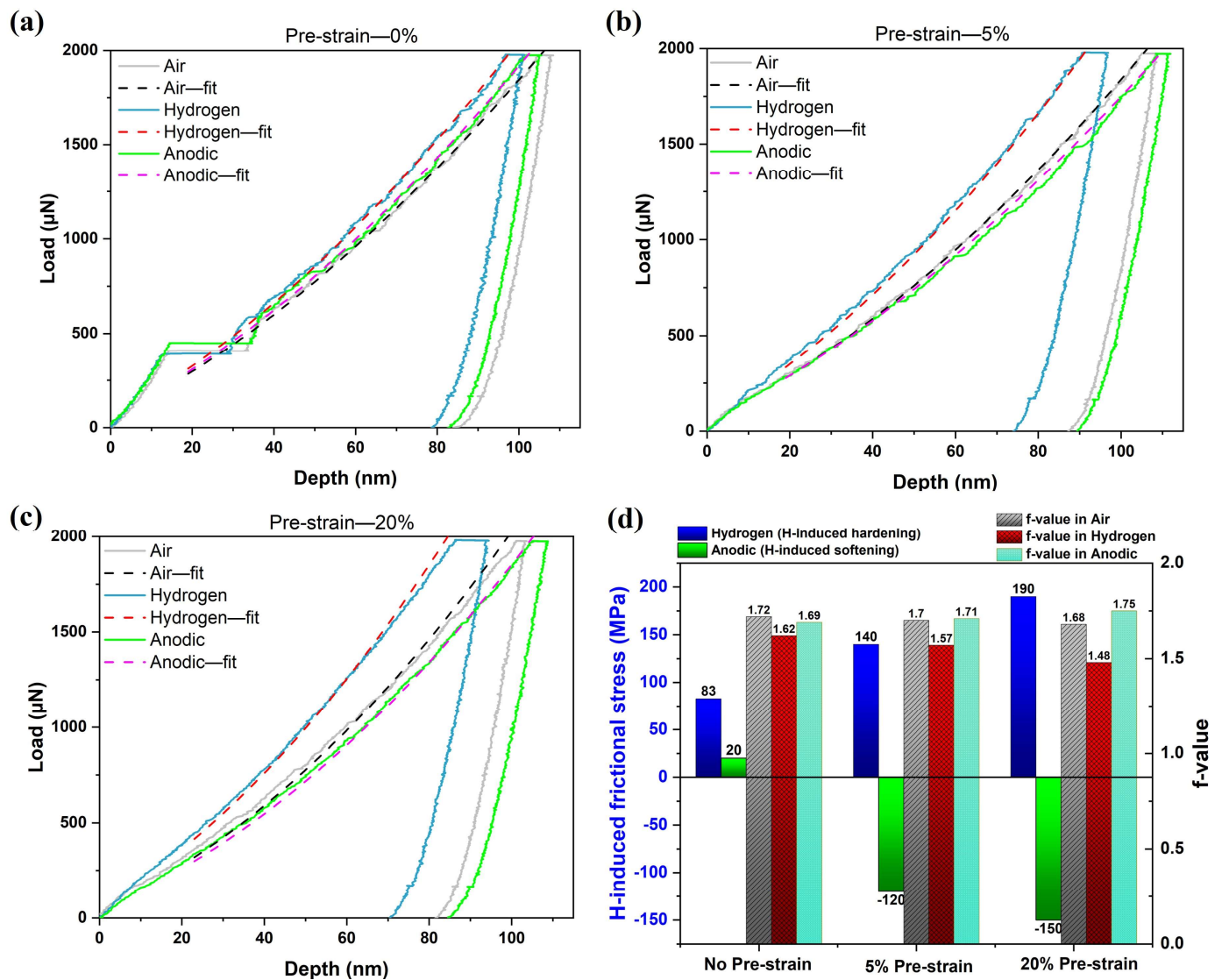


**Figure 4.** (a–c) The representative LD plot along with the fit data of the elastoplastic part for different pre-strain samples. (a) No pre-strain. (b) 5% pre-strain. (c) 20% pre-strain. (d) summary of results from elastoplastic modelling.

After one hour of anodic polarization, the positive contribution to the frictional stress is observed for the undeformed sample due to the presence of residual hydrogen (see Figure A1). In contrast, hydrogen-induced softening was observed during hydrogen degassing for the pre-strained samples. This indicates that surface modifications induced by hydrogen charging promote hydrogen absorption and further the formation of defects (vacancies and dislocations). The highest concentration of hydrogen and defects is anticipated for the 20% pre-strain sample. Those permanent defects induce a softening effect upon loading, and the frictional stress decreases as the concentration of defects increases (pre-strain increases). To understand this difference in the plastic's behavior, a TEM examination of indents is performed on the 5% pre-strain sample.

### 3.3. Hydrogen Effect on Plastic Deformation

The microstructure beneath the indent of the 5% pre-strained sample at three different conditions is shown in Figure 5. Though the material is pre-strained, the deformation induced by the indentation process is clearly distinguishable as a population of densely packed dislocations in the TEM images. In addition, the average kernel misorientation

(KAM) map of the same region also indicates profusely accumulated dislocations close to the indents (Figure 5g–i).

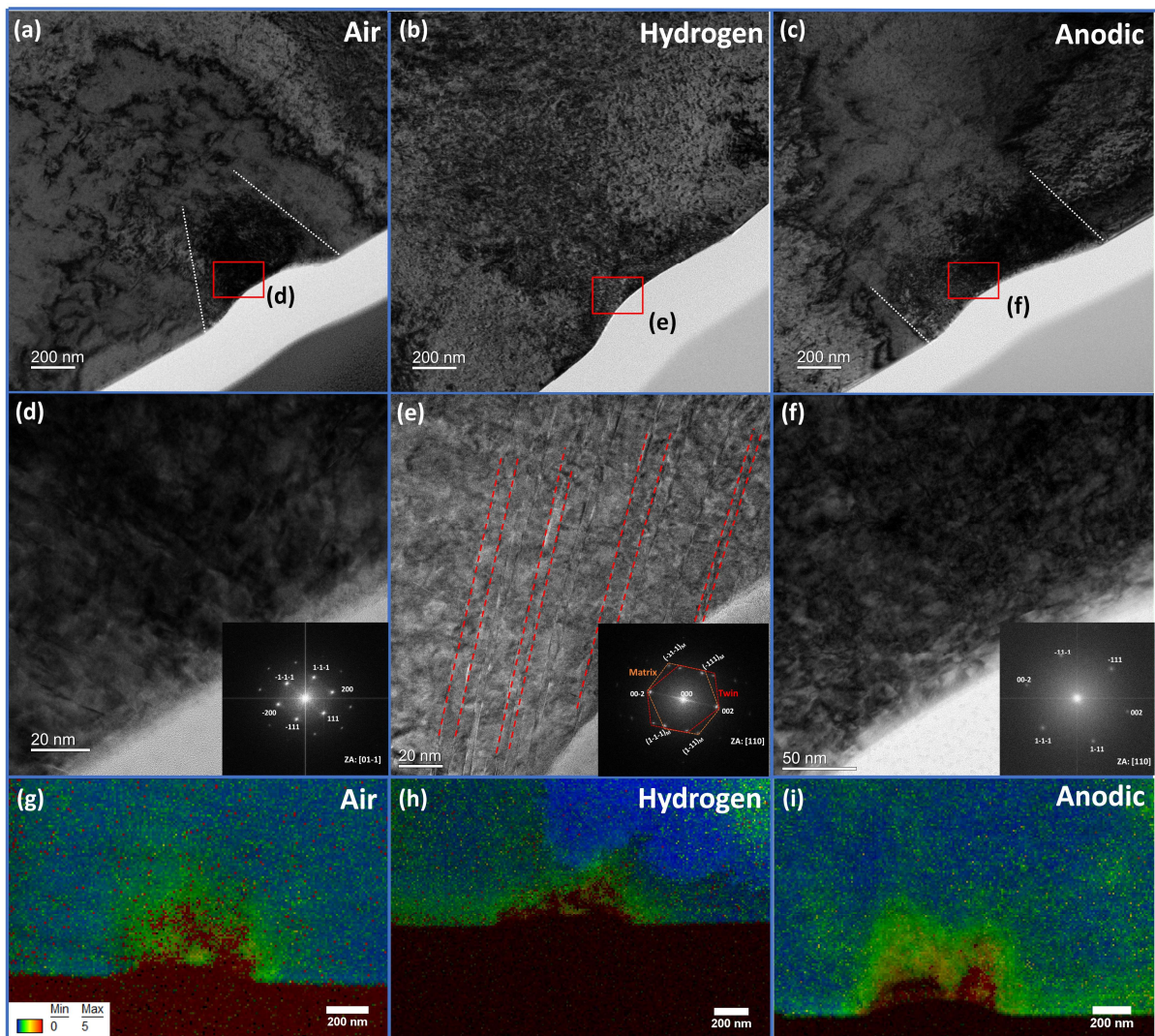


**Figure 5.** Bright field TEM microstructure (a–f) and Kernal average misorientation (KAM) map from the transmission Kikuchi diffraction (TKD) technique (g–i) for the indents corresponding to the 5% pre-strain sample: (a,d,g) indent in air, (b,e,h) hydrogen, and (c,f,i) anodic. (Some of the deformation twins are illustrated by red dashed lines in (e)).

The electron diffraction pattern for the hydrogen-charged sample indicates the presence of deformation twins at the indent region (inset in Figure 5e). In addition, the deformation zone is found to be confined to the indent region, suggesting that plastic deformation is localized (Figure 5h). The surface hydrogen concentration can be estimated by the relation  $C_s = \frac{\omega C_M}{4} \sqrt{\frac{\pi}{Dt}}$ . Here  $\omega$  is the thickness of the specimen,  $C_M$  is the total hydrogen concentration,  $t$  is the charging time, and  $D$  is the diffusion coefficient, which is taken as  $2.65 \times 10^{-15} \text{ m}^2/\text{s}$  for the present study [10]. For the 5% pre-strain sample, the surface concentration is estimated to be of 240 wt. ppm. Such a large mass fraction of hydrogen is sufficient to reduce the stacking fault energy (SFE) locally [32–34]. Moreover, the loading rate employed in the present work is  $8000 \mu\text{N}/\text{s}$ , and the hydrogen diffusion rate might not be sufficiently large enough to accommodate the applied strain rate and promote enhanced dislocation mobility. Thus, the high applied strain rate and dissolved hydrogen solute reducing SFE locally can collectively promote the twinning process as an alternative

accommodative mechanism in the pre-strained material. This is reflected in the hardness response, and it is reasonable to assume that the propensity to twin increases with the increasing pre-strain.

At variance with the hydrogen-charged case, the deformation zone is more pronounced under anodic conditions (Figure 5i), and even more so when it is compared to the indents performed in air, as one can see from the large deformation area on the KAM map. The deformation zone developed in air shows a spherical/tear drop shape that is confined to the cone of the material defined by the indenter impression (white dashed lines in Figure 5a). During indentation, the material tends to flow away from the indenter and the plastic flow is non-uniform due to the complex stress state underneath the indenter. Additionally, the nearby materials act to constrain the material flow, causing the plastic zone to expand radially from the center of the indent, resembling a rounded/tear drop shape. This is consistent with the expansion cavity model proposed by Johnson [25]. The deformation zone depth in the anodic sequence is comparable to that observed in air. However, its width is two times wider than it is in air. Additionally, the plastic zone resembles a parallel stacking of deformation layers (Figure 5c), as opposed to the commonly observed spherical cavity. The plausible explanation for this behavior is that the material has been compressed into either the voids or the atomic scale vacancies present in the microstructure.

The information from the anodic sequence offers a clear indication of microstructural changes caused by hydrogen. During anodic polarization, the hydrogen is removed from the subsurface, thereby leaving behind irreversible changes in pre-strained samples. Our study indicates that, during hydrogen charging, the pre-existing lattice defects promote hydrogen uptake and facilitate dislocation activity—as observed in the scanning probe microscopy images, after charging, in the form of slip lines (see Figure A2)—and thereby enhance strain-induced vacancy concentration. Thus, the decrease in hardness is due to hydrogen-induced vacancy enhancement through dislocation interactions in pre-strained samples [11,35,36]. Even though around 5% of residual hydrogen is present after the anodic sequence in pre-strained samples, the hydrogen-enhanced vacancy formation subdues the hardening effect. While, for the undeformed sample, the SPM image after charging (Figure A2) shows no significant change in surface morphology. The hydrogen charging condition employed is not sufficient to trigger irreversible microstructural changes. Therefore, the hardening effect observed after one hour of anodic desorption is due to the presence of residual hydrogen in the microstructure.

In our earlier work regarding in situ nanoindentation of undeformed nickel alloy 625, we showed evidence of hydrogen-enhanced vacancy formation upon charging at a high cathodic current density (of  $-1 \text{ mA/cm}^2$ ) followed by the anodic polarization sequence [30]. This was attributed to high internal stress generated at the surface due to the collective role of sluggish diffusion and supersaturation of hydrogen at the surface. The key difference in the present study is that, in the case of pre-strained material, an order smaller cathodic current density ( $-0.1 \text{ mA/cm}^2$ ) is sufficient to trigger a similar irreversible microstructural change.

The present findings strongly suggest that hydrogen interacts with pre-existing defects in an autocatalytic manner, i.e., tensile deformation-induced lattice defects promote further hydrogen uptake, which, in turn, facilitates the defect generation by reducing their formation energy [4,37], and this cycle repeats itself, manifesting eventually as a failure.

#### 4. Summary, Conclusions and Future Scopes

In this study, we explore the impact of hydrogen on pre-strained nickel alloy 625 using the in situ electrochemical nanoindentation technique. To unveil the interactions between hydrogen and material behavior, all differently pre-strained samples underwent similar hydrogen charging–desorption cycles followed by nanoindentation and microscopic observations.

During hydrogen incorporation, all the samples experienced hardening attributed to hydrogen solutes impeding dislocation motion. The hydrogen uptake enhanced by the

pre-strain results in a localized reduction in the stacking fault energy (SFE) and stimulates mechanical twinning at the surface, giving rise to an appreciable hardness increase. Conversely, pre-strained samples exhibited softening during the desorption cycle, attributed to the interaction of hydrogen solutes with pre-existing defects, causing irreversible microstructural changes in the form of hydrogen-enhanced vacancies.

Our study is not the only one to shed light on a familiar key observation—during electrochemical charging, hydrogen solutes interact with pre-existing defects leading to permanent microstructural changes through the creation of new crystal defects—but it also suggests that this process operates in an autocatalytic manner, potentially escalating hydrogen uptake and defect generation, ultimately influencing (accelerating) material failure.

To further advance the comprehension of hydrogen's impact on pre-existing defects and, consequently, the material integrity of nickel alloys in service, future research necessitates a comprehensive experimental approach. Precise defect concentration measurement through advanced techniques like electron microscopy, X-ray diffraction, and positron annihilation spectroscopy can be employed to assess the concentrations of dislocations, vacancies, and their complexes, respectively. By applying these methods before and after hydrogen charging and indentation, the concentration-dependent evolution of defects can be quantified. Additionally, when conducting in situ nanoindentation tests on samples, post-fatigue testing will prove valuable in investigating the hydrogen's effect on nanomechanical properties associated with specific dislocation patterns. To complement experimental investigations, the incorporation of simulation approaches, such as discrete dislocation dynamics and atomistic simulations, will provide a deeper understanding of the role of hydrogen and pre-existing defects on nanomechanical properties. Integrating time-resolved studies, examining environmental factors, exploring hydrogen diffusion, and validating simulation results against experimental data are essential aspects that should be considered in order to broaden the research scope and enhance its applicability to real-world conditions and industry applications.

**Author Contributions:** Conceptualization, C.K.S.; methodology, C.K.S., X.L. and D.W.; writing—original draft preparation, C.K.S.; writing—review and editing, C.K.S., X.L., D.W. and A.V.; supervision, A.V. All authors have read and agreed to the published version of the manuscript.

**Funding:** This work was supported by the Research Council of Norway and industries through the project M-HEAT (294689).

**Data Availability Statement:** The raw data supporting the conclusions of this article will be made available by the authors on request.

**Acknowledgments:** We appreciate the help of Per Erik Vullum for TEM investigations.

**Conflicts of Interest:** The authors declare no conflicts of interest.

## Appendix A. Relation Used to Plot Diffusion–Desorption Profile in Figure 2c

For the present study, prior to an indentation in hydrogen, the samples were charged at a constant current density of  $-0.1 \text{ mA/cm}^2$  for two hours, followed by one hour of anodic potential at  $0 \text{ mV}$ , in order to study the desorption effect. The simple diffusion–desorption relationship for two hours of charging and one hour of degassing is derived below.

Using a thin plate model from Ficks first law, the hydrogen distribution in the sample  $C_{(x,t)}$  can be calculated as:

$$\frac{C_{(x,t)} - C_0}{C_s - C_0} = 1 - \operatorname{erf}\left(\frac{x}{\sqrt{4Dt}}\right) \quad 0 < x < l \quad (\text{A1})$$

$$\operatorname{erf}(u) = \frac{2}{\pi} \int_0^u \exp(-u^2) du \quad (\text{A2})$$

where  $C_0$  is the initial hydrogen concentration,  $t$  is the charging time,  $D$  is the diffusion coefficient,  $l$  is the thickness of the sample, and  $\operatorname{erf}(u)$  denotes the error function. For

hydrogen discharging, the following relation is considered. Since the initial hydrogen distribution is non-uniform, a non-steady state equation, which accounts for constant surface concentration and initial distribution  $f'(x) = \frac{C(x,7200)}{C_s} = 1 - \operatorname{erf}\left(\frac{x}{\sqrt{4Dt}}\right)$   $0 < x < l$ , is considered for anodic discharging [13,30].

$$c(x,t) = c_1 + (c_2 - c_1)\frac{x}{l} + \frac{2}{\pi} \sum_1^{\infty} \frac{c_2 \cos n\pi - c_1}{n} \sin\left(\frac{n\pi x}{l}\right) \exp\left(-\frac{Dn^2\pi^2 t}{l^2}\right) + \frac{2}{l} \sum_1^{\infty} \sin\frac{n\pi x}{l} \exp\left(-\frac{Dn^2\pi^2 t}{l^2}\right) \int_0^1 f'(x) \sin\frac{n\pi x'}{l} dx' \quad (\text{A3})$$

with the boundary conditions:

$$c = c_1, x = 0, t \geq 0 \quad (\text{A4})$$

$$c = c_2, x = l, t \geq 0 \quad (\text{A5})$$

Here,  $c_1$  and  $c_2$  represent the hydrogen concentration at the position,  $x = 0$  and  $x = l$ , respectively, and  $n$  is the index of summation term. During the start of anodic polarization, it was tactically assumed that the surface concentration reaches zero, i.e.,  $c_1 = 0$ . Diffusion–desorption profiles for all samples are plotted using the above relations and shown in Figure A1.

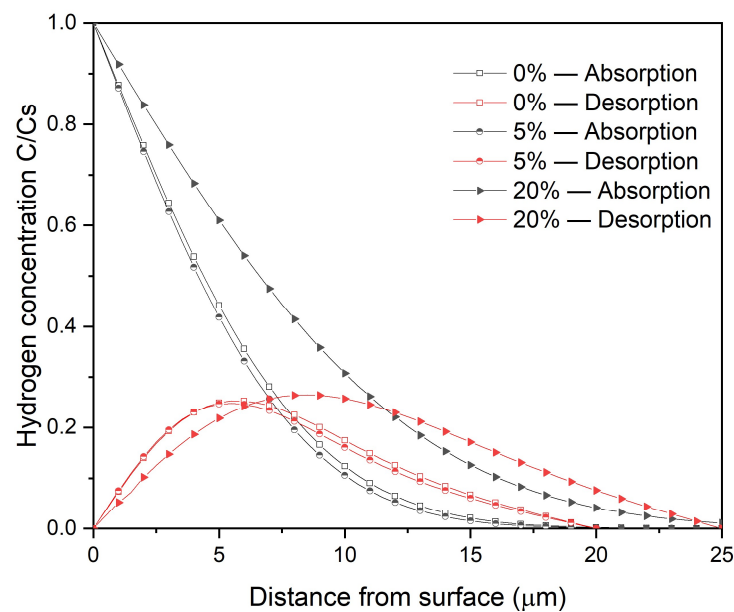


**Figure A1.** Diffusion–desorption profile for all the samples after two hours of charging and one hour of discharging.

**Table A1.** Hydrogen concentration at the depth of 650 nm estimated from the diffusion–desorption profile in Figure A1.

Sample	Diffusion Coefficient (m <sup>2</sup> /s) [10]	Discharged Hydrogen after Anodic Sequence (%)	Remaining Hydrogen after Anodic Sequence (%)
Undeformed	$2.93 \times 10^{-15}$	94.71	5.29
5% pre-strain	$2.65 \times 10^{-15}$	94.56	5.44
20% pre-strain	$6.67 \times 10^{-15}$	96.32	3.68

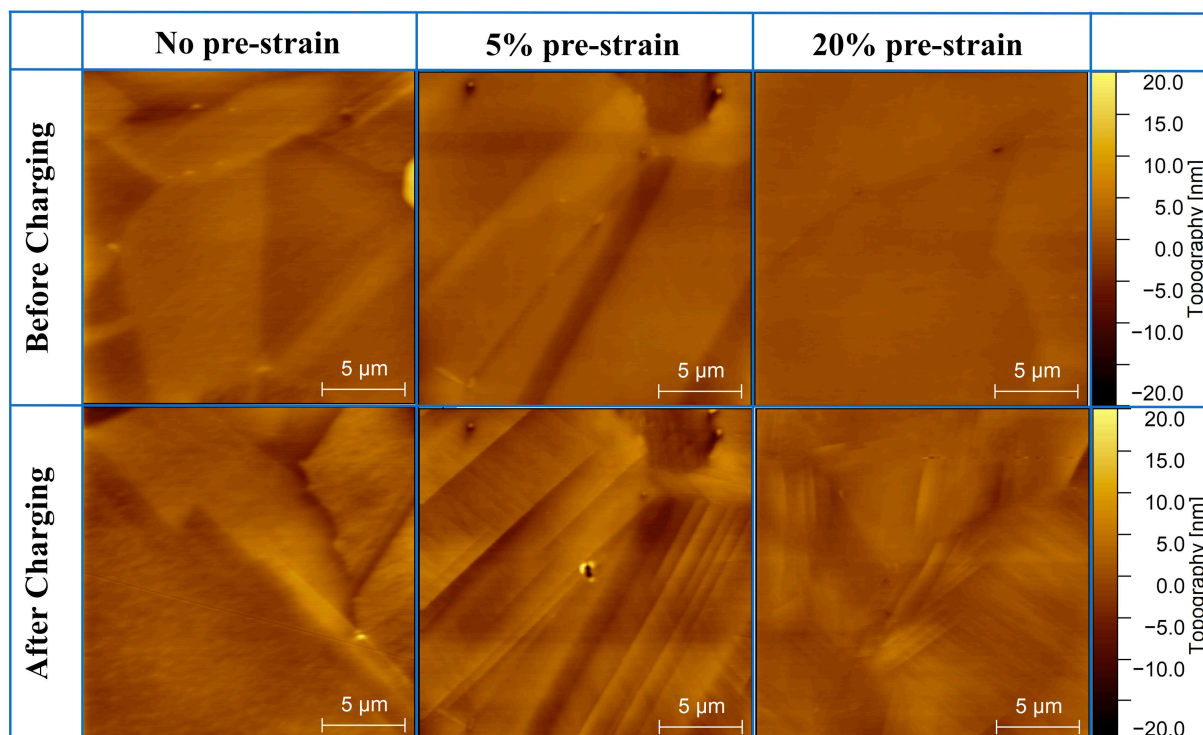


**Figure A2.** Scanning probe microscopy (SPM) images for various pre-strained samples before and after charging.

## References

- Robertson, I.M.; Sofronis, P.; Nagao, A.; Martin, M.L.; Wang, S.; Gross, D.W.; Nygren, K.E. Hydrogen Embrittlement Understood. *Metall. Mater. Trans. B* **2015**, *46*, 1085–1103. [\[CrossRef\]](#)
- Takai, K.; Shoda, H.; Suzuki, H.; Nagumo, M. Lattice Defects Dominating Hydrogen-Related Failure of Metals. *Acta Mater.* **2008**, *56*, 5158–5167. [\[CrossRef\]](#)
- Lynch, S.P. Hydrogen Embrittlement (HE) Phenomena and Mechanisms. In *Stress Corrosion Cracking*; Elsevier: Amsterdam, The Netherlands, 2011; pp. 90–130. ISBN 9781845696733.
- Kirchheim, R. Revisiting Hydrogen Embrittlement Models and Hydrogen-Induced Homogeneous Nucleation of Dislocations. *Scr. Mater.* **2010**, *62*, 67–70. [\[CrossRef\]](#)
- Ghermaoui, I.M.A.; Oudriss, A.; Metsue, A.; Milet, R.; Madani, K.; Feugas, X. Multiscale Analysis of Hydrogen-Induced Softening in f.c.c. Nickel Single Crystals Oriented for Multiple-Slips: Elastic Screening Effect. *Sci. Rep.* **2019**, *9*, 13042. [\[CrossRef\]](#)
- Hachet, G.; Oudriss, A.; Barnoush, A.; Milet, R.; Wan, D.; Metsue, A.; Feugas, X. The Influence of Hydrogen on Cyclic Plasticity of <001> Oriented Nickel Single Crystal. Part I: Dislocation Organisations and Internal Stresses. *Int. J. Plast.* **2020**, *126*, 102611. [\[CrossRef\]](#)
- Boniszewski, T.; Smith, G.C. The Influence of Hydrogen on the Plastic Deformation Ductility, and Fracture of Nickel in Tension. *Acta Metall.* **1963**, *11*, 165–178. [\[CrossRef\]](#)
- Metsue, A.; Oudriss, A.; Bouhattate, J.; Feugas, X. Contribution of the Entropy on the Thermodynamic Equilibrium of Vacancies in Nickel. *J. Chem. Phys.* **2014**, *140*, 104705. [\[CrossRef\]](#) [\[PubMed\]](#)
- Lawrence, S.K.; Yagodzinskyy, Y.; Hänninen, H.; Korhonen, E.; Tuomisto, F.; Harris, Z.D.; Somerday, B.P. Effects of Grain Size and Deformation Temperature on Hydrogen-Enhanced Vacancy Formation in Ni Alloys. *Acta Mater.* **2017**, *128*, 218–226. [\[CrossRef\]](#)
- Lu, X.; Díaz, A.; Ma, J.; Wang, D.; He, J.; Zhang, Z.; Johnsen, R. The Effect of Plastic Deformation on Hydrogen Diffusion in Nickel Alloy 625. *Scr. Mater.* **2023**, *226*, 115210. [\[CrossRef\]](#)
- Oudriss, A.; Martin, F.; Creus, J.; Bouhattate, J.; Marchetti, L.; Feugas, X. Contributions of Polarized Dislocation Walls, Internal Stresses and Vacancies on Hydrogen Trapping Processes in Tensile Strengthening (100) Nickel Single Crystal. *Acta Mater.* **2023**, *245*, 118622. [\[CrossRef\]](#)
- Lu, X.; Ma, Y.; Peng, D.; Johnsen, R.; Wang, D. In situ Nanomechanical Characterization of Hydrogen Effects on Nickel-Based Alloy 725 under Different Metallurgical Conditions. *J. Mater. Sci. Technol.* **2022**, *135*, 156–169. [\[CrossRef\]](#)
- Wang, D.; Lu, X.; Deng, Y.; Guo, X.; Barnoush, A. Effect of Hydrogen on Nanomechanical Properties in Fe-22Mn-0.6C TWIP Steel Revealed by in-situ Electrochemical Nanoindentation. *Acta Mater.* **2019**, *166*, 618–629. [\[CrossRef\]](#)
- Yang, G.; Zhao, Y.; Lee, D.H.; Park, J.M.; Seok, M.Y.; Suh, J.Y.; Ramamurty, U.; Jang, J.I. Influence of Hydrogen on Incipient Plasticity in CoCrFeMnNi High-Entropy Alloy. *Scr. Mater.* **2019**, *161*, 23–27. [\[CrossRef\]](#)

15. Hachet, G.; Oudriss, A.; Barnoush, A.; Hajilou, T.; Wang, D.; Metsue, A.; Feaugas, X. Antagonist Softening and Hardening Effects of Hydrogen Investigated Using Nanoindentation on Cyclically Pre-Strained Nickel Single Crystal. *Mater. Sci. Eng. A* **2021**, *803*, 140480. [[CrossRef](#)]
16. Zhao, Y.; Lee, D.H.; Kim, W.J.; Seok, M.Y.; Kim, J.Y.; Han, H.N.; Suh, J.Y.; Ramamurty, U.; Jang, J.I. Influence of Pre-Strain on the Gaseous Hydrogen Embrittlement Resistance of a High-Entropy Alloy. *Mater. Sci. Eng. A* **2018**, *718*, 43–47. [[CrossRef](#)]
17. Reddy, K.S.; Govindaraj, Y.; Neelakantan, L. Hydrogen Diffusion Kinetics in Dual-Phase (DP 980) Steel: The Role of Pre-Strain and Tensile Stress. *Electrochim. Acta* **2023**, *439*, 141727. [[CrossRef](#)]
18. Hadam, U.; Zakroczymski, T. Absorption of Hydrogen in Tensile Strained Iron and High-Carbon Steel Studied by Electrochemical Permeation and Desorption Techniques. *Int. J. Hydrogen Energy* **2009**, *34*, 2449–2459. [[CrossRef](#)]
19. Barnoush, A.; Vehoff, H. Recent Developments in the Study of Hydrogen Embrittlement: Hydrogen Effect on Dislocation Nucleation. *Acta Mater.* **2010**, *58*, 5274–5285. [[CrossRef](#)]
20. Nibur, K.; Bahr, D.; Somerday, B. Hydrogen Effects on Dislocation Activity in Austenitic Stainless Steel. *Acta Mater.* **2006**, *54*, 2677–2684. [[CrossRef](#)]
21. Oliver, W.C.; Pharr, G.M. An Improved Technique for Determining Hardness and Elastic Modulus Using Load and Displacement Sensing Indentation Experiments. *J. Mater. Res.* **1992**, *7*, 1564–1583. [[CrossRef](#)]
22. Chauniyal, A.; Dehm, G.; Janisch, R. On the Role of Pre-Existing Defects in Influencing Hardness in Nanoscale Indentations—Insights from Atomistic Simulations. *J. Mech. Phys. Solids* **2021**, *154*, 104511. [[CrossRef](#)]
23. Morris, J.R.; Bei, H.; Pharr, G.M.; George, E.P. Size Effects and Stochastic Behavior of Nanoindentation Pop In. *Phys. Rev. Lett.* **2011**, *106*, 165502. [[CrossRef](#)] [[PubMed](#)]
24. Bei, H.; Xia, Y.Z.; Barabash, R.I.; Gao, Y.F. A Tale of Two Mechanisms: Strain-Softening versus Strain-Hardening in Single Crystals under Small Stressed Volumes. *Scr. Mater.* **2016**, *110*, 48–52. [[CrossRef](#)]
25. Johnson, K. *Contact Mechanics*; Cambridge University Press: Cambridge, UK, 1987.
26. Barnoush, A. Correlation between Dislocation Density and Nanomechanical Response during Nanoindentation. *Acta Mater.* **2012**, *60*, 1268–1277. [[CrossRef](#)]
27. Song, J.; Curtin, W.A. Mechanisms of Hydrogen-Enhanced Localized Plasticity: An Atomistic Study Using  $\alpha$ -Fe as a Model System. *Acta Mater.* **2014**, *68*, 61–69. [[CrossRef](#)]
28. Ogawa, Y.; Hosoi, H.; Tsuzaki, K.; Redarce, T.; Takakuwa, O.; Matsunaga, H. Hydrogen, as an Alloying Element, Enables a Greater Strength-Ductility Balance in an Fe-Cr-Ni-Based, Stable Austenitic Stainless Steel. *Acta Mater.* **2020**, *199*, 181–192. [[CrossRef](#)]
29. Gu, Y.; El-Awady, J.A. Quantifying the Effect of Hydrogen on Dislocation Dynamics: A Three-Dimensional Discrete Dislocation Dynamics Framework. *J. Mech. Phys. Solids* **2018**, *112*, 491–507. [[CrossRef](#)]
30. Soundararajan, C.K.; Wang, D.; Vinogradov, A. Effect of Hydrogen on Nanomechanical Properties of Inconel 625 Studied Using In-situ Electrochemical Nanoindentation Technique. *J. Alloys Compd.* **2023**, *948*, 169742. [[CrossRef](#)]
31. Nix, W.D.; Gao, H. Indentation Size Effects in Crystalline Materials: A Law for Strain Gradient Plasticity. *J. Mech. Phys. Solids* **1998**, *46*, 411–425. [[CrossRef](#)]
32. Ferreira, P.J.; Robertson, I.M.; Birnbaum, H.K. Hydrogen Effects on the Interaction between Dislocations. *Acta Mater.* **1998**, *46*, 1749–1757. [[CrossRef](#)]
33. Pontini, A.E.; Hermida, J.D. X-ray Diffraction Measurement of the Stacking Fault Energy Reduction Induced by Hydrogen in an AISI 304 Steel. *Scr. Mater.* **1997**, *37*, 1831–1837. [[CrossRef](#)]
34. Zhang, C.; Zhi, H.; Antonov, S.; Chen, L.; Su, Y. Hydrogen-Enhanced Densified Twinning (HEDT) in a Twinning-Induced Plasticity (TWIP) Steel. *Scr. Mater.* **2021**, *190*, 108–112. [[CrossRef](#)]
35. Sugiyama, Y.; Takai, K. Quantities and Distribution of Strain-Induced Vacancies and Dislocations Enhanced by Hydrogen in Iron. *Acta Mater.* **2021**, *208*, 116663. [[CrossRef](#)]
36. Fukai, Y.; Shizuku, Y.; Kurokawa, Y. Superabundant Vacancy Formation in Ni-H Alloys. *J. Alloys Compd.* **2001**, *329*, 195–201. [[CrossRef](#)]
37. Kirchheim, R. Solid Solution Softening and Hardening by Mobile Solute Atoms with Special Focus on Hydrogen. *Scr. Mater.* **2012**, *67*, 767–770. [[CrossRef](#)]

**Disclaimer/Publisher’s Note:** The statements, opinions and data contained in all publications are solely those of the individual author(s) and contributor(s) and not of MDPI and/or the editor(s). MDPI and/or the editor(s) disclaim responsibility for any injury to people or property resulting from any ideas, methods, instructions or products referred to in the content.